TTMP vol 2 (3), 2025
doi: 10.30511/TTMP.2025.2061851.1055

Transactions in Theoretical
and Mathematical Physics

Advancing numerical solutions to analytical form through the hybrid analytical and numerical method

Ali Ahmadi Azar [1, a]

[a] Department of Mechanical Engineering, NT.C., Islamic Azad University, Tehran, Iran

Received: 26 May 2025 / Accepted: 25 August 2025 / Published: 26 August 2025

Abstract Analytical solutions of differential equations provide exact representations of physical phenomena, enhance computational efficiency, and offer deeper theoretical insights than purely numerical approaches. In mathematical physics, such solutions are essential for uncovering fundamental laws, accurately predicting system behavior, and developing closed-form expressions that drive further theoretical advancements and physical interpretations. However, the complexity of real-world differential equations—with their inherent nonlinearities, variable coefficients, and intricate boundary conditions—often precludes the attainment of exact analytical solutions, resulting in the predominance of numerical methods that offer computational feasibility albeit at the cost of precision. This study aims to overcome these limitations by employing the hybrid analytical and numerical method (HAN method) to derive an analytical solution for the nonlinear differential equation (NDE) governing Jeffery–Hamel flow. Initially, numerical solutions of the governing equations are obtained to construct a comprehensive dataset, which, together with the boundary conditions, facilitates the extraction and formulation of an exact analytical solution. This HAN method effectively upgrades numerical approximations into analytical forms, thereby bridging the gap between computational practicality and theoretical rigor in the analysis of complex NDEs.

1 Introduction

1.1 Significance of the HAN method

Realistic modelling of natural phenomena often leads to highly nonlinear differential equations characterized by coplex nonlinearities, variable coefficients, and challenging boundary conditions. Although numerical methods are prevalently used to approximate solutions for these equations, their outputs are typically approximate and may lack the precise theoretical insights offered by analytical solutions. The HAN method addresses this gap by initially employing numerical techniques to obtain approximate solutions and subsequently converting these results into closed-form analytical expressions. This approach leverages the computational efficiency of numerical methods while ultimately providing the exactness and interpretability of analytical solutions, thereby offering a unique and effective framework for solving complex NDEs.

1.2 Literature review

A growing body of literature has focused on the HAN method as a novel approach to overcoming the challenges posed by NDEs. Several recent studies have demonstrated that the HAN method not only enhances computational efficiency by leveraging numerical approximations but also facilitates the extraction of precise analytical solutions that offer deeper theoretical insights. These investigations collectively underscore the potential of the HAN method to bridge the gap between conventional numerical techniques and exact analytical formulations in mathematical physics. A pioneering study [1] introduces the HAN method that converts numerical approximations of the NDEs into closed - form analytical solutions. The study investigates complex physical phenomena such as heat and mass transfer, momentum transport, and electromagnetic effects in fluid systems, where intricate nonlinearities and challenging boundary conditions often hinder direct analytical treatment. By leveraging numerical data to systematically extract analytical expressions, the HAN method overcomes these difficulties while delivering enhanced computational efficiency and precision. This approach bridges the gap between the practical benefits of numerical techniques and the deep theoretical insights offered by analytical solutions, thereby advancing the understanding of the underlying physics in mathematical modeling. In another study [2], the combined effects of thermo-diffusion, electric fields, and nonlinear thermal radiation on the steady flow of an incompressible non-Darcy Casson fluid over a vertical permeable stretchable plate were examined. The researchers employed the HAN method

---

[1] E-mail: aliahmadiazar.mech@gmail.com, a.ahmadi.azar@iau-tnb.ac.ir

to simplify the governing nonlinear partial differential equations (PDEs) into the ordinary differential equations (ODEs) through the similarity transformations (STs), demonstrating significant influences of Casson's parameter, magnetic fields, and electric fields on velocity, temperature, and concentration distributions. Additionally, the study analyzed the roles of thermal buoyancy, porous permeability, Eckert and Prandtl numbers, and chemical reactions, offering valuable insights for industrial applications involving heat transfer in non-Newtonian fluids. Another research [3] demonstrates that the HAN Method is employed to analyze the steady magnetohydrodynamic (MHD) flow of a non-Newtonian Reiner-Rivlin viscoelastic fluid confined between two parallel plates. The governing PDEs are converted into the ODEs using Von Kármán STs, and the HAN Method is applied to solve these equations analytically, with results validated against Homotopy Perturbation Method (HPM) and Runge-Kutta numerical solutions. The research further presents new quantitative findings derived from the HAN solutions, contributing to the understanding of MHD viscoelastic fluid dynamics in constrained geometries. In another study [4], researchers investigated the transient three-dimensional flow of nanomaterial thin films over a rotating angled plate by transforming the governing PDEs into nonlinear ODEs using similarity variables. The study employed modified Akbari-Ganji Method (AGM) and HAN method to solve the equations, with results validated against numerical Runge-Kutta solutions. The analysis examined key dimensionless parameters across four distinct cases, demonstrating the effectiveness of these semi-analytical approaches for complex rotating flow systems. In another study [5], researchers analysed the steady two-dimensional flow of micropolar fluids between permeable porous walls using two analytical methods to solve the nonlinear governing equations. The study revealed that key dimensionless parameters, such as coupling and spin gradient viscosity, significantly influence flow characteristics, while micro-inertia density and Peclet numbers selectively affect microrotation, temperature, and concentration profiles. The work provides novel physical insights into micropolar fluid dynamics, particularly the distinct responses of dimensionless parameters to varying flow conditions. In another study [6], researchers developed an analytical solution for the Emden-Chandrasekhar equation (ECE) in the stellar structures theory (SST). Using the HAN method, addressing a longstanding challenge in modelling polytropic stellar structures. The HAN-method provided explicit solutions for density, mass, and pressure across all regions of a star, unlike prior approaches limited to the stellar core, and introduced a dimensionless fundamental constant ($\alpha = 0.1719381834$) critical to the SST. The results, validated against experimental models, accurately predicted properties of the Sun, including its average temperature ($1.0305 \times 107\text{K}$), demonstrating the method's robustness for astrophysical applications. In another study [7], researchers analysed the unsteady, two-dimensional flow of a temperature-dependent non-Newtonian (Casson) MHD fluid through an expandable/contractible channel with permeable plates. Using similarity transformations and the HAN method, the governing nonlinear PDEs were reduced to ODEs, revealing how key parameters (R and A) influence velocity profiles ($F(\xi)$, $F'(\xi)$) and temperature ($\theta(\xi)$), with suction/injection effects quantified. The study's novelty lies in its 3D/2D contour visualization of parameter variations and analysis of local skin friction and Nusselt number, validated against prior work. In another theoretical study [8], magnetohydrodynamic flow of a conducting micropolar fluid between two stretching disks was examined, with particular focus on how structural modifications (disk spacing and stretching rate) influence fluid dynamics. The analysis employed similarity transformation- ns and the HAN-method to redefine five key dimensionless parameters, connecting mathematical solutions with physical behaviour; results showed increased stretching rates sharply elevate temperature and Nusselt number, while greater disk spacing reduces microrotation and wall stress. Validation against previous work confirmed direct correlations between structural adjustments and changes in velocity profiles, thermal properties, and micro-rotation characteristics, yielding practical insights for engineering applications. In another theoretical study [9], steady laminar flow of an incompressible micropolar fluid between a porous upper disk and a solid lower disk was investigated, with governing equations reduced to ODEs via Von-Karman transformations. The study employed the Modified AGM and HAN method—novel analytical approaches for this unsolved problem—to examine how slip coefficients, Reynolds number, and micropolar parameters (vortex viscosity, spin gradient viscosity, microinertia density) affect velocity and microrotation profiles. Results, validated against existing data, revealed consistent outcomes between both methods while providing new physical insights into the system's behaviour under varying parametric conditions. In another theoretical study [10], an exact solution was derived for von Kármán swirling flow induced by an infinite-radius rotating disk with uniform suction, examining two scenarios: co-directional and opposing far-field swirl. Using similarity transformations and the HAN method, the study analysed three cases-(1) swirl without suction, (2) suction without swirl, and (3) combined effects—revealing that skin friction peaks when far-field angular velocity is negligible (Case 1) and increases with suction intensity (Case 2). The results further demonstrated that pressure reduces to a distance-dependent function when key parameters ($s = a = 0$) vanish, providing new insights into viscous flow dynamics under rotational and suction boundary conditions. Another study [11] applied the HAN method to analyse MHD hyperbolic tangent nanofluid flow over a permeable wedge, converting governing equations into ODEs containing critical dimensionless parameters. Results demonstrated that while fluid velocity showed strong dependence on Weissenberg number and magnetic effects, heat and mass transfer rates (Nusselt/Sherwood numbers) remained largely unaffected by most parameters except local Reynolds number. The research provided new understanding of parameter interactions in wedge flows, particularly regarding skin friction variations and the relative insensitivity of thermal and concentration boundary layers to many controlling factors. In another study [12], three analytical methods were employed to analyse time-dependent MHD oscillatory flow and heat transfer in an asymmetric wavy porous channel, with the pressure gradient treated as a complex function generating both real and imaginary solutions. The results demonstrated that while parameters like the Hartmann number and porous medium shape factor strongly influenced real fluid velocity, only radiation affected both real velocity and temperature profiles, with imaginary components responding uniquely to frequency and Peclet number variations. This work's significance lies in its novel approach to solving complex differential equations, validated by the remarkable agreement between all three methods' solutions, offering new precision in modelling wavy-channel flow dynamics. In another study [13], a novel analytical approach was developed to investigate flow and heat transfer in planar Taylor–Couette systems, where a rotating inner cylinder interacts with a hotter stationary outer cylinder. By transforming nonlinear PDEs into ODEs using simplifying assumptions and a penalty function replacement for pressure, the study revealed key dynamics—including a pronounced tangential velocity gradient, efficient inward heat transfer ($Nu = 1.58$ inner/-0.58 outer cylinder), and entropy generation adhering to thermodynamic laws. The work's significance lies in its quantitative validation of Taylor-Couette flow at $Re = 900$ and $Pr = 6.9$, coupled with insights into skin friction coefficients and entropy distribution, advancing the understanding of such systems beyond traditional numerical methods. In another theoretical study [14], the Klein-Gordon equation with a $\lambda\varphi^4$ interaction and symmetry-breaking term was analysed in the context of a generalized uncertainty principle incorporating minimal length scales, addressing quantum gravity predictions. The HAN method was employed to solve the resulting Euler-Lagrange equation (ELE), providing a framework to quantify corrections to scalar field systems under these modified physical assumptions. This work bridges quantum gravity phenomenology with practical computational techniques, offering insights into how Planck-scale effects might manifest in field-theoretic systems. In another study [15], the unsteady flow of a temperature-dependent Casson fluid through an expandable/contractible porous channel was analyzed using the HAN method. The results demonstrated that wall expansion increased maximum fluid velocity by 19.07% while raising average temperature by 100.92%, with the Casson parameter and Prandtl number showing significant but contrasting effects on velocity (4.7% increase) and temperature (51.5% decrease) profiles respectively. This work provides novel quantitative insights into non-Newtonian fluid behavior in deformable porous media, offering practical guidance for thermal-fluid system design in engineering applications. In another study [16], the century-old Von Kármán swirling flow problem was revisited using the innovative HAN method to derive highly accurate semi-analytical solutions. This approach uniquely combines numerical computations with analytical formulations, enabling precise calculation of key physical parameters like boundary layer thickness, shear stress, and moment coefficients that were previously challenging to determine. The work demonstrates both mathematical innovation in solving nonlinear differential equations and practical advancements in fluid mechanics analysis, particularly for rotating disk systems. In another study [17], boundary layer flow and heat transfer of a dusty hyperbolic tangent fluid over a stretching sheet were analyzed, with particular focus on thermal radiation and magnetic field effects. Using the HAN-method to solve transformed nonlinear ODEs, the research revealed that radiation significantly increases both fluid and dust-phase temperatures (e.g., fluid temperature rose 180% without magnetic field, 190% with field) while leaving velocities unaffected, with magnetic fields amplifying these thermal effects. These findings provide critical insights for industrial thermal management systems, especially in nuclear cooling and high-temperature processes where precise control of non-Newtonian fluid behavior is essential.

1.3 Problem statement

Building upon the justification for using the HAN method in Section 1.1 and the literature review in Section 1.2, this study investigates the steady, unidirectional flow of an incompressible viscous fluid emanating from a source or sink at the intersection of two rigid plane walls with an included angle of 2α where α is the angle of the channel which is in term of degree. For the divergent channel, α is considered positive ($\alpha > 0$) and for the convergent channel, α is considered negative ($\alpha < 0$). The governing equations for this physical system are derived in Section 2, while Section 3 details the application of the HAN method to solve these equations. Parametric analysis of the flow characteristics including the investigation of the different Reynolds numbers in both divergent and convergent channels is presented in Section 4, with key findings and conclusions summarized in Section 5.

2 Governing equation

2.1 Problem overview

The analysis considers the steady, incompressible flow of a viscous fluid emanating from (or converging toward) a source (or sink) situated at the junction of two rigid plane walls. These walls form a wedge characterized by a total angle of 2α. A cylindrical polar coordinate system is employed here, wherein the coordinates (r,θ,z) are defined; however, because the flow is assumed to be two-dimensional and confined to a plane, the z-direction is not considered. In this system, r denotes the radial distance from the origin, and θ represents the angular position. The flow is assumed to be purely radial, meaning that the tangential velocity component u_θ is zero ($u_\theta = 0$) and the radial component u_r is the dominant contributor. Variations in u_r depends on both the variables r and θ, that is: $u_r = u_r(r, \theta)$. This formulation is applicable to engineering applications where the fluid behavior in nonparallel channels must be accurately modeled. The two-dimensional convergent channel configuration (see Figure 1) illustrates a case where the channel contracts, thereby intensifying the flow toward the vertex. Conversely, the divergent channel configuration (see Figure 2) repre- sents an expanding channel where the flow disperses outward from the source.

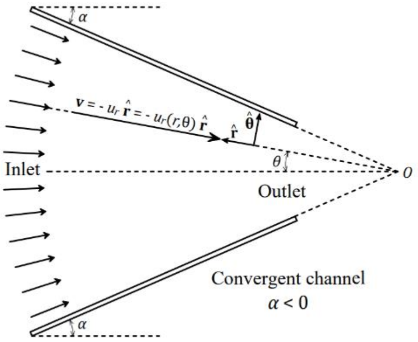

Fig. 1 Two-dimensional schematic diagram illustrating a convergent channel where the flow is directed inward toward a narrowing region, typical of a fluid sink configuration.

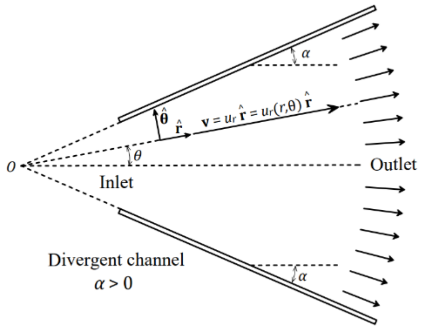

Fig. 2 Two-dimensional schematic diagram depicting a divergent channel where the flow originates from a common vertex and expands outward, typical of a fluid source configuration.

2.2 Derivation of Jeffery-Hamel flow governing equations

The Jeffery-Hamel flow describes the steady, incompressible, laminar flow of a viscous fluid between two nonparallel plane walls meeting at an angle 2α (the angle of both convergent and divergent channel is twice the angle of each wall with respect to r-axis). This flow is characterized by a purely radial velocity field, where fluid emanates from or converges toward the apex of the wedge-shaped channel. The derivation of its governing equations involves simplifying the Navier-Stokes equations under symmetry assumptions and eliminating the pressure field through mathematical consistency. In the current Section, a detailed derivation presentation tailored for readers new to this Jeffery-Hamel flow. As illustrated in Figures 1 and 2, the Jeffery–Hamel flow is governed by the steady, incompressible Navier-Stokes equations. Given the nature of the flow, the cylindrical coordinate system is the most suitable framework for its mathematical representation. Before stating the simplifications assumptions, let us demonstrate the more general form of the equations as below [18, 19]:

$$\frac{\mathrm{D}\rho}{\mathrm{D}t} + \rho\boldsymbol{\nabla}\cdot\mathbf{v} = 0, \tag{1}$$

$$\rho\frac{\mathrm{D}\mathbf{u}}{\mathrm{D}t} = -\nabla p + \mu\nabla^2\mathbf{u} + \mathbf{F}, \tag{2}$$

where $\mathrm{D}/\mathrm{D}t$ is total derivative of with respect to time, $\mathbf{u} = u_r\hat{\mathbf{r}} + u_\theta\hat{\boldsymbol{\theta}}$ is the velocity vector of the fluid, ρ is density of fluid, μ is the dynamic viscosity of the fluid, p is the pressure distribution, u_r is the radial velocity of fluid, u_θ is the azimuthal velocity of fluid, and $\mathbf{F}$ is the body force per unit volume. The Jeffery–Hamel flow in this study is considered steady, incompressible, constant viscosity, two-dimensional, and without any body forces per unit volume such as gravity or magnetic field. In addition to these assumptions, the azimuthal velocity of fluid is ignored $(u_\theta = u_\theta(r,\theta) = 0)$ in this study and the flow is purely along radial axis $(u_r = u_r(r,\theta) \neq 0)$. Therefore, Eqs. (1) and (2) reduced to the following forms:

$$\frac{1}{r}\frac{\partial}{\partial r}(ru_r) = \frac{u_r}{r} + \frac{\partial u_r}{\partial r} = 0, \tag{3}$$

$$\rho u_r\frac{\partial u_r}{\partial r} = -\frac{\partial p}{\partial r} + \mu\left(\frac{\partial^2 u_r}{\partial r^2} + \frac{1}{r}\frac{\partial u_r}{\partial r} - \frac{u_r}{r^2} + \frac{1}{r^2}\frac{\partial^2 u_r}{\partial\theta^2}\right), \tag{4}$$

$$\frac{\partial p}{\partial\theta} = \frac{2\mu}{r}\frac{\partial u_r}{\partial\theta}, \tag{5}$$

where PDEs (3)-(5) are the governing equations of the Jeffery–Hamel flow and the boundary conditions of this flow is as follows:

$$u_r(r,\pm\alpha) = 0, \tag{6}$$

$$u_r(r,\theta)|_{\theta=0} = \frac{L_{\mathrm{char}}U_{\max}}{r}, \tag{7}$$

$$\left.\frac{\partial u_r(r,\theta)}{\partial\theta}\right|_{\theta=0} = 0. \tag{8}$$

The pressure distribution in this problem is not constant and it is function both r and θ $(p = p(r,\theta) \neq 0)$. The pressure $p(r,\theta)$ appears in both Eqs. 4-5, but it is not a primary variable of interest. To simplify the Jeffery-Hamel PDEs

(3)-(5), the pressure by enforcing consistency between the radial and angular momentum equations through cross-differentiation should be eliminated. By doing so, the first step is to start with the radial momentum equation and differentiate both sides of Eq. (4) with respect to the variable θ:

$$\rho\left(\frac{\partial u_r}{\partial \theta}\frac{\partial u_r}{\partial r}+u_r\frac{\partial^2 u_r}{\partial \theta \partial r}\right)=-\frac{\partial^2 p}{\partial \theta \partial r} +\mu\left(\frac{\partial^3 u_r}{\partial \theta \partial r^2}+\frac{1}{r}\frac{\partial^2 u_r}{\partial \theta \partial r}-\frac{1}{r^2}\frac{\partial u_r}{\partial \theta}+\frac{1}{r^2}\frac{\partial^3 u_r}{\partial \theta^3}\right), \tag{9}$$

where $\partial^2 p/\partial \theta \partial r$ can simply determine from Eq. (9) as below:

$$\frac{\partial^2 p}{\partial \theta \partial r}=\mu\left(\frac{\partial^3 u_r}{\partial \theta \partial r^2}+\frac{1}{r}\frac{\partial^2 u_r}{\partial \theta \partial r}-\frac{1}{r^2}\frac{\partial u_r}{\partial \theta}+\frac{1}{r^2}\frac{\partial^3 u_r}{\partial \theta^3}\right) -\rho\left(\frac{\partial u_r}{\partial \theta}\frac{\partial u_r}{\partial r}+u_r\frac{\partial^2 u_r}{\partial \theta \partial r}\right). \tag{10}$$

The second step is to start with the angular momentum result and differentiate both sides of Eq. (5) with respect to the variable r:

$$\frac{\partial^2 p}{\partial r \partial \theta}=-\frac{2\mu}{r^2}\frac{\partial u_r}{\partial \theta}+\frac{2\mu}{r}\frac{\partial^2 u_r}{\partial r \partial \theta}. \tag{11}$$

For a smooth pressure field, mixed partial derivatives must be equal:

$$\frac{\partial^2 p}{\partial \theta \partial r}=\frac{\partial^2 p}{\partial r \partial \theta}. \tag{12}$$

So, by substituting the Eqs. (10) and (11) into Eq. (12), yields the following equation:

$$\underbrace{\mu\left(\frac{\partial^3 u_r}{\partial \theta \partial r^2}+\frac{1}{r}\frac{\partial^2 u_r}{\partial \theta \partial r}+\frac{1}{r^2}\frac{\partial u_r}{\partial \theta}+\frac{1}{r^2}\frac{\partial^3 u_r}{\partial \theta^3}\right)}_{\text{Viscous terms}} =\underbrace{\rho\left(\frac{\partial u_r}{\partial \theta}\frac{\partial u_r}{\partial r}+u_r\frac{\partial^2 u_r}{\partial \theta \partial r}\right)}_{\text{Inertial terms}}. \tag{13}$$

The continuity equation (3) and momentum equations (4) and (5), along with their corresponding boundary conditions (6)-(8), have been simplified but remain analytically challenging to solve. One effective approach to facilitate their solution is to reduce the number of independent variables. By introducing a similarity variable, η, in place of the original variables r and θ, the partial differential equations (PDEs) governing Jeffery-Hamel flow can be transformed into a single nonlinear ordinary differential equation (ODE). This simplification significantly enhances the tractability of the problem while preserving its physical essence.

The similarity variables that can do that, are as below [20-31]:

$$F(\eta):=\frac{f(\theta)}{L_{\text{char}}U_{\max}}=\frac{r u_r(r,\theta)}{L_{\text{char}}U_{\max}}, \quad \eta:=\frac{\theta}{\alpha}, \tag{14}$$

where in Eq. (14), $U_{\max}=U_{\text{char}}$ and also the similarity variable in Eq. (14) is satisfied in the continuity equation (3), which is showed in Eq. (15):

$$\frac{1}{r}\frac{\partial}{\partial r}\left(r\frac{f(\theta)}{r}\right)=\frac{1}{r}\cdot 0=0. \tag{15}$$

Applying the similarity variables of Eq. (14) in Eq. (13), will results the ODE form of Eq. (13). Thus, the both viscous and inertial terms changed as follows, respectively:

$$\begin{aligned}\mu\left(\frac{\partial^3 u_r}{\partial \theta \partial r^2}+\frac{1}{r}\frac{\partial^2 u_r}{\partial \theta \partial r}+\frac{1}{r^2}\frac{\partial u_r}{\partial \theta}+\frac{1}{r^2}\frac{\partial^3 u_r}{\partial \theta^3}\right) &=\mu\left(\frac{2L_{\text{char}}U_{\max}}{r^3\alpha}\frac{\mathrm{d}F(\eta)}{\mathrm{d}\eta}+\frac{L_{\text{char}}U_{\max}}{r^3\alpha}\frac{\mathrm{d}F(\eta)}{\mathrm{d}\eta}\right.\\ &\quad\left.+\frac{L_{\text{char}}U_{\max}}{r^3\alpha}\frac{\mathrm{d}F(\eta)}{\mathrm{d}\eta}+\frac{L_{\text{char}}U_{\max}}{r^3\alpha^3}\frac{\mathrm{d}^3F(\eta)}{\mathrm{d}\eta^3}\right)\\ &=\frac{\mu L_{\text{char}}U_{\max}}{r^3}\left(\frac{4}{\alpha}\frac{\mathrm{d}F(\eta)}{\mathrm{d}\eta}+\frac{1}{\alpha^3}\frac{\mathrm{d}^3F(\eta)}{\mathrm{d}\eta^3}\right).\end{aligned} \tag{16}$$

$$\begin{aligned}\rho\left(\frac{\partial u_r}{\partial \theta}\frac{\partial u_r}{\partial r}+u_r\frac{\partial^2 u_r}{\partial r \partial \theta}\right) &=\rho\left\{\left[\frac{L_{\text{char}}U_{\max}}{r\alpha}\frac{\mathrm{d}F(\eta)}{\mathrm{d}\eta}\right]\left[-\frac{L_{\text{char}}U_{\max}}{r^2}F(\eta)\right]\right.\\ &\quad\left.+\left[\frac{L_{\text{char}}U_{\max}}{r}F(\eta)\right]\left[-\frac{L_{\text{char}}U_{\max}}{r^2\alpha}\frac{\mathrm{d}F(\eta)}{\mathrm{d}\eta}\right]\right\}\\ &=-\frac{\rho(L_{\text{char}}U_{\max})^2}{r^3\alpha}\left[F(\eta)\frac{\mathrm{d}F(\eta)}{\mathrm{d}\eta}+F(\eta)\frac{\mathrm{d}F(\eta)}{\mathrm{d}\eta}\right]\\ &=-\frac{2\rho(L_{\text{char}}U_{\max})^2}{r^3\alpha}F(\eta)\frac{\mathrm{d}F(\eta)}{\mathrm{d}\eta}.\end{aligned} \tag{17}$$

Thus, the results of substituting the similarity variable (14) into momentum equation (13) is showed in Eqs. (16) and (17). By substituting them, the following dimensional ODE will be determined:

$$\frac{\mu L_{\text{char}}U_{\max}}{r^3}\left(\frac{4}{\alpha}\frac{\mathrm{d}F(\eta)}{\mathrm{d}\eta}+\frac{1}{\alpha^3}\frac{\mathrm{d}^3F(\eta)}{\mathrm{d}\eta^3}\right) =-\frac{2\rho(L_{\text{char}}U_{\max})^2}{r^3\alpha}F(\eta)\frac{\mathrm{d}F(\eta)}{\mathrm{d}\eta}, \tag{18}$$

where Eq. (18) is the simpler form of Eq. (13). By multiply the $r^3/\mu L_{\text{char}}U_{\max}$ in Eq. (18), will make this ODE, dimensionless as below:

$$\frac{4}{\alpha}\frac{\mathrm{d}F(\eta)}{\mathrm{d}\eta}+\frac{1}{\alpha^3}\frac{\mathrm{d}^3F(\eta)}{\mathrm{d}\eta^3} = -\frac{2\rho L_{\mathrm{char}}U_{\max}}{\mu\alpha}F(\eta)\frac{\mathrm{d}F(\eta)}{\mathrm{d}\eta}, \tag{19}$$

where multiplying the α^3 in both sides of Eq. (19), the following dimensionless ODE will be achieved:

$$\frac{\mathrm{d}^3F(\eta)}{\mathrm{d}\eta^3}+2\alpha ReF(\eta)\frac{\mathrm{d}F(\eta)}{\mathrm{d}\eta}+4\alpha^2\frac{\mathrm{d}F(\eta)}{\mathrm{d}\eta}=0, \tag{20}$$

where Re in Eq. (20) is the Reynolds number is defined in Eq. (21):

$$Re=\frac{\alpha\rho L_{\mathrm{char}}U_{\max}}{\mu}. \tag{21}$$

In many published studies [20-31], the similarity variable of Eq. (14) is used by them and they derived the dimensionless ODE of the Jeffery-Hamel flow exactly like Eq. (20). Again, by applying the similarity variables (14) on boundary conditions (BCs) of the PDEs (6)-(8) and making them dimensionless, the following boundary conditions are derived:

$$F(\eta)|_{\eta=0}=1, \quad \left.\frac{\mathrm{d}F(\eta)}{\mathrm{d}\eta}\right|_{\eta=0}=0, \quad F(\eta)|_{\eta=1}=0. \tag{22}$$

Now the BCs (22) are appropriate for the Jeffery–Hamel equation (which is showed in Eq. (20)).

3 The application of HAN method

The HAN method represents a groundbreaking approach in computational mathematics, first introduced by A. Ahmadi Azar [16, 17]. It is distinguished as the first technique capable of transforming numerical solutions into analytical forms, thereby resolving convergence issues and mitigating the unwieldy increase in the number of terms typical of many analytical solutions. In essence, the HAN method achieves an analytical solution with a remarkably concise representation.

A further strength of this method is its inherent flexibility. When a nonlinear differential equation defies solution by a specific numerical method, the HAN method can seamlessly incorporate an alternative numerical approach to generate the desired solution. At its core, the method unfolds in five systematic steps. First, an analytical solution is postulated in the form of a power series or polynomial featuring constant yet undetermined coefficients. These coefficients are then determined by solving a system of algebraic equations that arise from the BCs of the differential equations—a procedure encapsulated in the second step.

Typically, the number of unknown coefficients needs the number of equations derivable directly from the given boundary conditions. To bridge this gap, additional approximated boundary conditions are introduced in the third step based on numerical solutions. This practical adaptation highlights the method's versatility, as it is not restricted to any specific numerical technique. In the fourth step, these approximated conditions are employed to formulate sufficient algebraic equations, and finally, the resulting linear system is solved to obtain the semi-analytical solution of the differential equation.

By successfully combining numerical and analytical techniques, the HAN method liberates researchers from the constraints of conventional analytical methods, offering a robust framework for deriving concise analytical solutions from numerical data.

In steps three and five, the method inherently assumes the validity of the results, so explicit validation is not initially addressed. Nevertheless, to rigorously confirm correctness, one can demonstrate the convergence of the numerical solution between steps three and four. Furthermore, substituting the derived analytical solution back into the differential equation enables an evaluation of the residual error—which, if the solution is accurate, remains negligible.

In our study, we implemented the Runge-Kutta method in Python to solve the differential equation, and we verified the convergence of the computed results to support the accuracy of our approach. Ultimately, executing all five steps and reinserting the analytical solution into the original equation conclusively substantiates the validity of the results.

This comprehensive verification framework not only bolsters the reliability of the HAN method but also underscores its potential for yielding precise solutions in complex computational scenarios.

According to the five steps that HAN method has, let us assume an analytical solution (ansatz) with constant but unknown coefficients for the Jeffery-Hamel equation (20) as follows:

$$F(\eta)=\sum_{i=0}^{11}a_i\eta^i, \tag{23}$$

where a_i in Eq. (23) represents 12 unknown coefficients the unknown. These unknown coefficients can be determined only when a system of consisting 12 algebraic equations constructed. The analytical solution that is already defined in the Eq. (23) is the first step of HAN method. The second step is to use the boundary conditions of the Jeffery-Hamel equation (20) which they are existed in Eq. (22) to make algebraic equations as follows:

$$F(\eta)|_{\eta=0}=\sum_{i=0}^{11}a_i\eta^i\Big|_{\eta=0}=1, \tag{24}$$

$$\left.\frac{\mathrm{d}F(\eta)}{\mathrm{d}\eta}\right|_{\eta=0} = \sum_{i=1}^{11} i a_i \eta^{i-1}\Big|_{\eta=0} = 0, \tag{25}$$

$$F(\eta)|_{\eta=1} = \sum_{i=0}^{11} a_i \eta^{i}\Big|_{\eta=1} = 0. \tag{26}$$

It is obvious that the number of Eqs. (24)-(26) are not enough to construct a system of algebraic equations. In order to construct additional algebraic equations, the numerical solution of the Jeffery-Hamel equation (۲۰) with its boundary conditions (۲۲) should be calculated which is the third step in the HAN method. The numerical solving of Eq. (۲۰) with its boundary conditions (۲۲) is successfully done via “*Fourth-order Implicit Runge-Kutta Collocation Method (Lobatto IIIA Formula) with Adaptive Mesh Refinement*”. Why the name this numerical method is like this? The answer is written in the following reasons:

- Implicit Runge-Kutta Framework: The method is based on an implicit Runge-Kutta formulation. Unlike explicit methods, it solves for the solution at multiple, interdependent collocation points simultaneously. This inherent implicitness grants excellent stability properties, particularly in stiff or complex boundary value problems like the one in your code.
- Collocation Approach: In a collocation method, the solution is approximated by a polynomial that is forced to satisfy the differential equation at a set of predefined points (the collocation points). This guarantees that the residual (error in satisfying the ODE) is nearly zero at those points, leading to a highly accurate overall solution.
- Lobatto IIIA Formula: The Lobatto IIIA variant is a specific choice for the collocation points and weights. A distinguishing feature is that this formula includes the endpoints of the integration interval, making it ideally suited for boundary value problems. It also confers additional symmetry and stability properties to the scheme.
- Fourth-order Accuracy: The method achieves fourth-order accuracy, meaning the local error decreases in proportion to the step size raised to the fourth power ($O(h^4)$). This level of accuracy strikes a balance between computational effort and precision, making it robust for many practical problems.
- Adaptive Mesh Refinement: The solver doesn’t rely on a fixed grid; it adapts the mesh based on error estimates. Regions where the solution changes rapidly get more refined mesh points, whereas smoother areas use fewer points. This adaptive approach enhances both efficiency and accuracy by focusing computational power where it’s needed most.

Each part of the name highlights a key element of the solver’s design, and together they describe a method that is stable, accurate, and efficient for solving boundary value problems. The shorter name of this numerical method is “*Fourth-order Lobatto IIIA Collocation Method with Adaptive Mesh Refinement*”. Thus, according to this code, the approximated boundary conditions or the numerical solution of the Jeffery-Hamel equation (۲۰) with its boundary conditions (۲۲) are calculated as follows:

Table 1 The numerical solution of the Jeffery-Hamel equation via Python for the scenario that $\alpha = 30°$ and $Re = 10$.

η	$F(\eta)$	$\mathrm{d}F(\eta)/\mathrm{d}\eta$	$\mathrm{d}^2F(\eta)/\mathrm{d}\eta^2$
0.0	1.000000	0.000000	-4.308476
0.1	0.978666	-0.422594	-4.063804
0.2	**0.917061**	**-0.798136**	-3.384597
0.3	0.821856	-1.089728	-2.413316
0.4	**0.702610**	**-1.277112**	-1.330752
0.5	0.570009	-1.357724	-0.301810
0.6	**0.434249**	**-1.343074**	0.560922
0.7	0.303917	-1.252785	1.207615
0.8	**0.185483**	**-1.108688**	1.641027
0.9	0.083311	-0.930512	1.896907
1.0	0.000000	**-0.733586**	2.024627

The Figures 3-5 shows the plots of $F(\eta)$, $\mathrm{d}F(\eta)/\mathrm{d}\eta$, and $\mathrm{d}^2F(\eta)/\mathrm{d}\eta^2$ respectively. However, the validity of the current numerical solution is showed by the residual of the numerical solution in Figure 6.

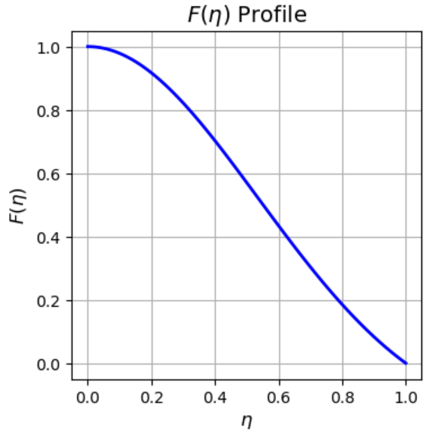

Fig. 3 The numerical solution of $F(\eta)$ by Python.

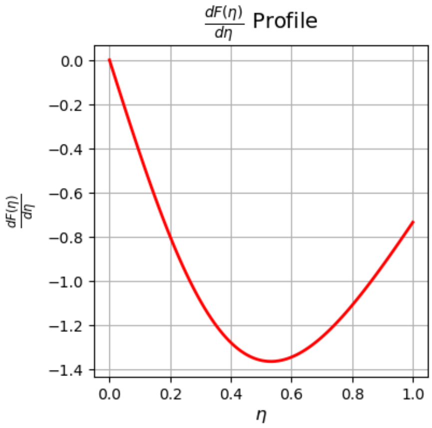

Fig. 4 The numerical solution of $\mathrm{d}F(\eta)/\mathrm{d}\eta$ by Python.

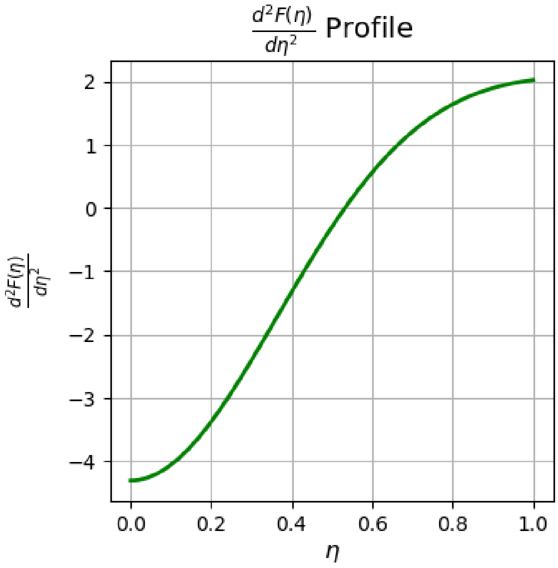

Fig. 5 The numerical solution of $\mathrm{d}^2F(\eta)/\mathrm{d}\eta^2$ by Python.

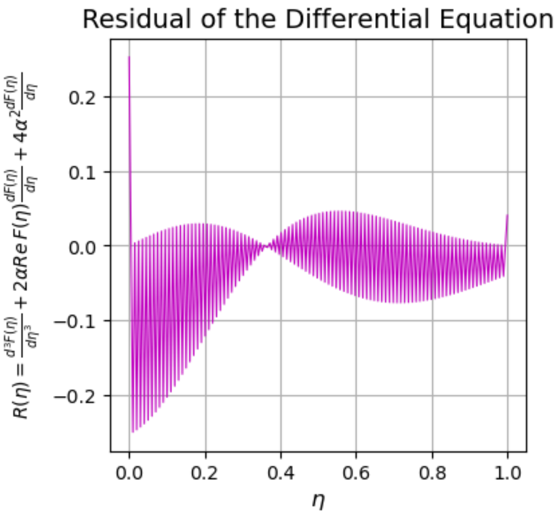

Fig. 6 The residual of numerical solution by Python.

The bold values in Table 1 are the approximated boundary conditions that are used in step four to make the rest of remaining algebraic equations as follows:

$$F(\eta)|_{\eta=0.2} = \sum_{i=0}^{11} a_i\eta^i\Big|_{\eta=0.2} = 0.917061, \tag{27}$$

$$\left.\frac{\mathrm{d}F(\eta)}{\mathrm{d}\eta}\right|_{\eta=0.2} = \sum_{i=1}^{11} ia_i\eta^{i-1}\Big|_{\eta=0.2} = -0.798136, \tag{28}$$

$$F(\eta)|_{\eta=0.4} = \sum_{i=0}^{11} a_i\eta^i\Big|_{\eta=0.4} = 0.702610, \tag{29}$$

$$\left.\frac{\mathrm{d}F(\eta)}{\mathrm{d}\eta}\right|_{\eta=0.4} = \sum_{i=1}^{11} ia_i\eta^{i-1}\Big|_{\eta=0.4} = -1.277112, \tag{30}$$

$$F(\eta)|_{\eta=0.6} = \sum_{i=0}^{11} a_i\eta^i\Big|_{\eta=0.6} = 0.434249, \tag{31}$$

$$\left.\frac{\mathrm{d}F(\eta)}{\mathrm{d}\eta}\right|_{\eta=0.6} = \sum_{i=1}^{11} ia_i\eta^{i-1}\Big|_{\eta=0.6} = -1.343074, \tag{32}$$

$$F(\eta)|_{\eta=0.8} = \sum_{i=0}^{11} a_i\eta^i\Big|_{\eta=0.8} = 0.185483, \tag{33}$$

$$\left.\frac{\mathrm{d}F(\eta)}{\mathrm{d}\eta}\right|_{\eta=0.8} = \sum_{i=1}^{11} ia_i\eta^{i-1}\Big|_{\eta=0.8} = -1.108688, \tag{34}$$

$$\left.\frac{\mathrm{d}F(\eta)}{\mathrm{d}\eta}\right|_{\eta=1} = \sum_{i=1}^{11} ia_i\eta^{i-1}\Big|_{\eta=1} = -0.733586, \tag{35}$$

where Eqs. (24)-(26) with addition to the Eqs. (27)-(35) are constructing a system of linear algebraic equation with 12 algebraic equations and 12 unknowns. By solving this system of linear algebraic equations in fifth step, the unknown coefficients in Eq. (36) will be determined as below:

$$\begin{array}{ll} a_0 = +1.000000, & a_1 = +\,0.000000, \\ a_2 = -\,2.153993, & a_3 = -\,0.001129, \\ a_4 = +2.091526, & a_5 = -\,0.107366, \\ a_6 = -\,1.135709, & a_7 = -\,1.364453, \\ a_8 = \ +3.745790, & a_9 = -\,3.081673, \\ a_{10} = +1.194394, & a_{11} = -0.187388, \end{array} \tag{36}$$

with substituting the known coefficients in Eq. (36), the following polynomial solution will be achieved for the Jeffery-Hamel equation (20) with its boundary conditions (22):

$$\begin{aligned} F(\eta) = \ & -0.187388\,\eta^{11} + \ 1.194394\eta^{10} \\ & - 3.081673\,\eta^{9} + 3.745790\,\eta^{8} \\ & - 1.364453\,\eta^{7} - \ 1.135709\,\eta^{6} \\ & - 0.107366\,\eta^{5} + \ 2.09152\ 6\eta^{4} \\ & - 0.001129\,\eta^{3} - \ 2.153993\,\eta^{2} \\ & + 1.000000\,. \end{aligned} \tag{37}$$

The Figures 7-9 shows the plots of $F(\eta)$, $\mathrm{d}F(\eta)/\mathrm{d}\eta$, and $\mathrm{d}^2F(\eta)/\mathrm{d}\eta^2$ from HAN solution (37), respectively.

However, the validity of the current analytical solution is showed by the residual of the HAN solution in Figure 10.

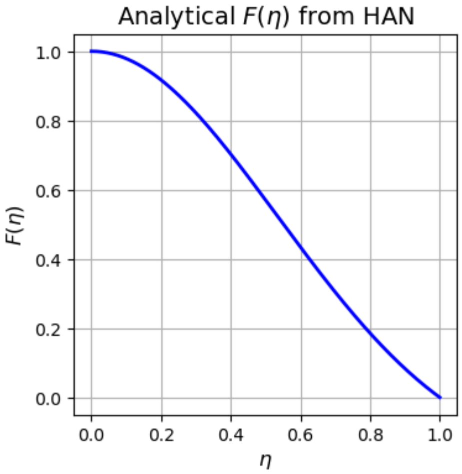

Fig. 7 The HAN solution of $F(\eta)$ by Python.

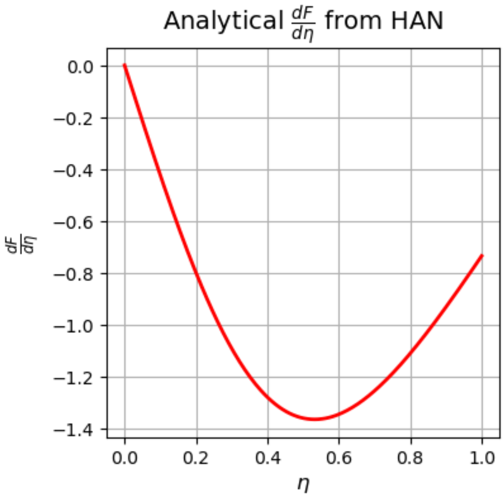

Fig. 8 The HAN solution of $\mathrm{d}F(\eta)/\mathrm{d}\eta$ by Python.

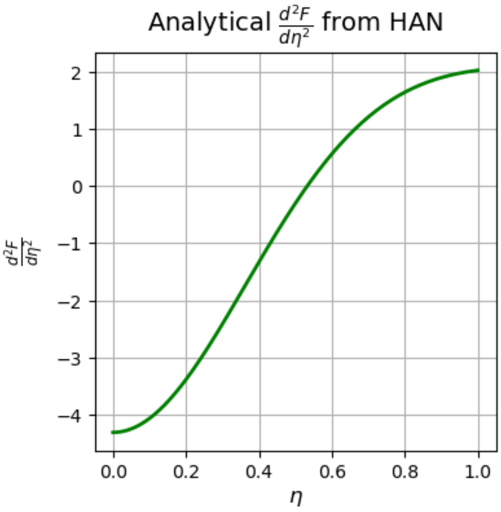

Fig. 9 The HAN solution of $\mathrm{d}^2F(\eta)/\mathrm{d}\eta^2$ by Python.

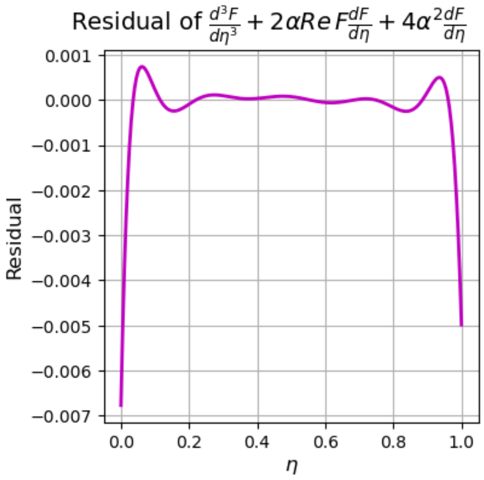

Fig. 10 The residual of HAN solution.

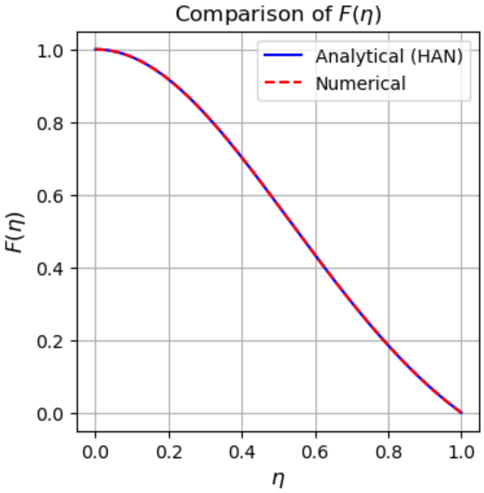

Fig. 11 The comparison between the HAN and numerical solutions of $F(\eta)$.

The validity of results is proved two times when the residuals of the both numerical and analytical solutions are showed in Figures 6 and 10. However, it is obvious that the graphs of HAN solution are significantly same as each other. Thus, the Figures 11-13 are showing the comparison of these two methods and finally Figures 14-16 shows how much is the error between HAN and the numerical solution is. Also, the calculated errors in Figures 14-16 are achieved with the help of the following relation:

$$PE = \left(\frac{|\text{Analytical} - \text{Numerical}|}{|\text{Numerical}|}\right) \times 100\%, \tag{38}$$

where PE is Percentage Error and the formula in Eq. (38) calculates percentage error relative to the maximum magnitude of the numerical solution to avoid division-by-zero issues and contextualize errors across the domain. By taking the absolute difference between analytical (HAN) and numerical values (|Analytical - Numerical|), it captures the raw deviation. Dividing by the absolute value of the numerical solution (|Numerical|) normalizes the error relative to the scale of the problem, ensuring stability even near zero-crossings. Multiplying by 100 converts this ratio into a percentage, providing an intuitive measure of how large the error is compared to the solution's peak magnitude. This approach balances sensitivity to local errors with robustness against numerical instabilities.

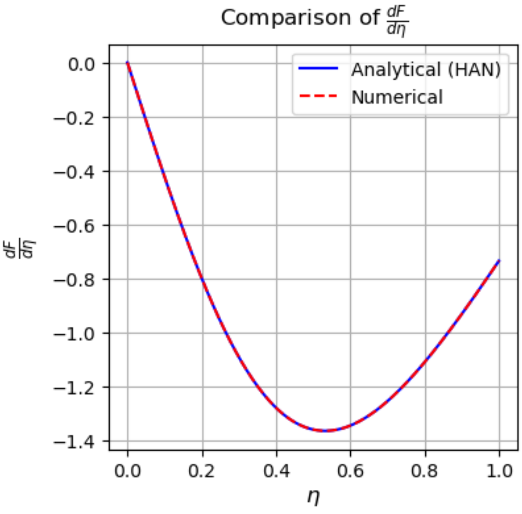

Fig. 12 The comparison between the HAN and numerical solutions of $\mathrm{d}F(\eta)/\mathrm{d}\eta$.

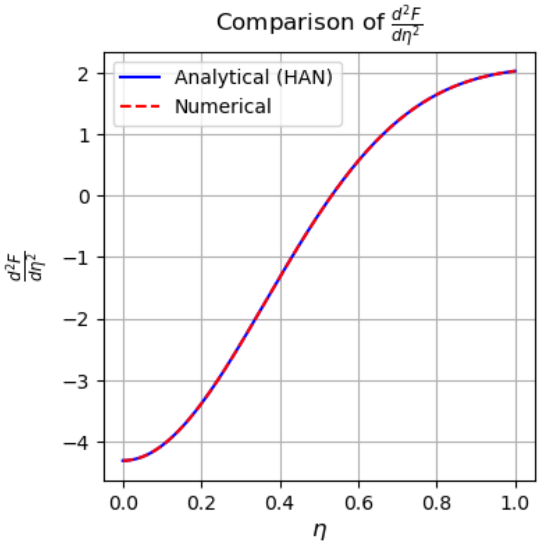

Fig. 13 The comparison between the HAN and numerical solutions of $\mathrm{d}^2F(\eta)/\mathrm{d}\eta^2$.

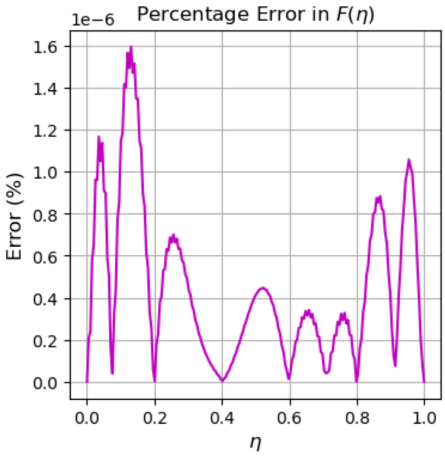

Fig. 14 The error between the HAN and numerical solutions for $F(\eta)$.

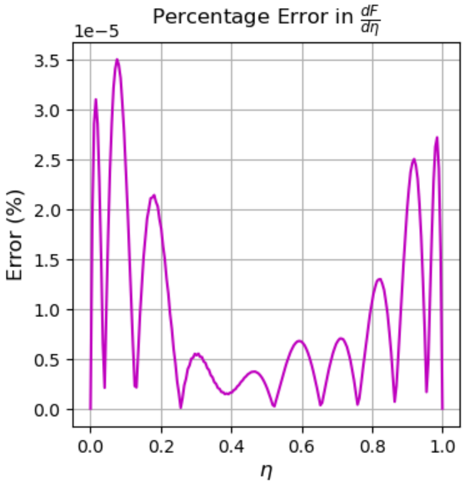

Fig. 15 The error between the HAN and numerical solutions for $\mathrm{d}F(\eta)/\mathrm{d}\eta$.

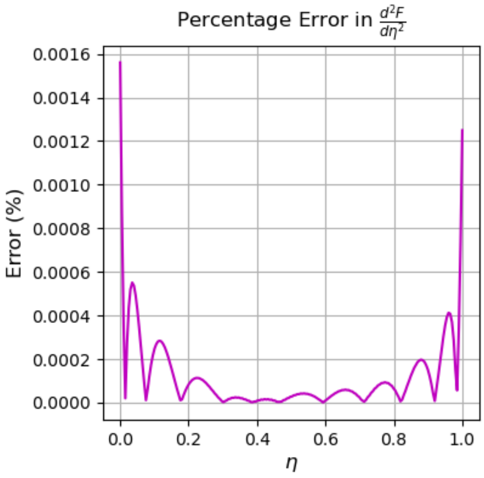

Fig. 16 The error between the HAN and numerical solutions for $\mathrm{d}^2F(\eta)/\mathrm{d}\eta^2$.

4 Results and discussion

4.1 Constitutive equations for the average value and percentage change

Before presenting the results and discussion, the average value of $F(\eta)$—representing the HAN solution for the Jeffery–Hamel flow described in Eq. (20)—along with its variation relative to a reference value is displayed as follows:

$$F_{\text{avg}} = \int_0^1 F(\eta)\mathrm{d}\eta. \tag{39}$$

$$\%\text{Change} = \frac{\text{Average}_{\text{new}} - \text{Average}_{\text{old}}}{\text{Average}_{\text{old}}} \times 100. \tag{40}$$

In Eq. (39), F_{avg} denotes the average value of $F(\eta)$ and %Change in Eq. (40), represents the percentage variation corresponding to a specific change.

4.2 Impact of Reynolds number and angle of wall in a divergent channel

4.2.1 Plot comparison of $\boldsymbol{F(\eta)}$ for different positive angles at fixed $\boldsymbol{Re}$

In the present subsection, a specific flow configuration is examined by analysing an incompressible fluid with constant velocity—which results in a constant Reynolds number—as the wall angle in a divergent channel increase. Quantitative results are presented in Tables 2–4. These tables indicate that as the channel's wall angle increases, the average fluid velocity decreases. This trend is consistent across all Reynolds numbers; however, Figures 17–19 and Tables 2–4 reveal that the decrease in velocity is more pronounced at higher Reynolds numbers. In other words, higher Reynolds numbers exhibit greater sensitivity to variations in the channel wall angles. Alternatively, when the wall angles decrease—approaching a configuration resembling a channel with flat walls—the average fluid velocity increases, with the effect being markedly stronger at high Reynolds numbers. Thus, for a given Reynolds number in a diverging channel, larger wall angles lead to lower average fluid velocities, while smaller angles result in higher average velocities. From an engineering perspective, among a range of positive channel angles, the largest angle produces the lowest velocity, and the smallest positive angle produces the highest velocity. It is important to note that differential equation (Eq. 20) is applicable only for channels that are either convergent ($\alpha < 0$) or divergent ($\alpha > 0$). At angles of 0°, 90°, 180°, or 360°, the channel is neither convergent nor divergent, and consequently, Jeffery–Hamel's equation (Eq. 20) cannot be applied.

Table 2 The quantitative results for for different positive angles when $Re = 5$.

α (deg)	F_{avg} (Average $F(\eta)$)	% Change (vs α = 5°)
5	0.659	0.0%
15	0.641	-2.7%
30	0.606	-8.1%

Table 3 The quantitative results for for different positive angles when $Re = 10$.

α (deg)	F_{avg} (Average $F(\eta)$)	% Change (vs α = 5°)
5	0.652	0.0%
15	0.617	-5.3%
30	0.550	-15.6%

Table 4 The quantitative results for for different positive angles when $Re = 20$.

α (deg)	F_{avg} (Average $F(\eta)$)	% Change (vs α = 5°)
5	0.637	0.0%
15	0.564	-11.4%
30	0.431	-32.3%

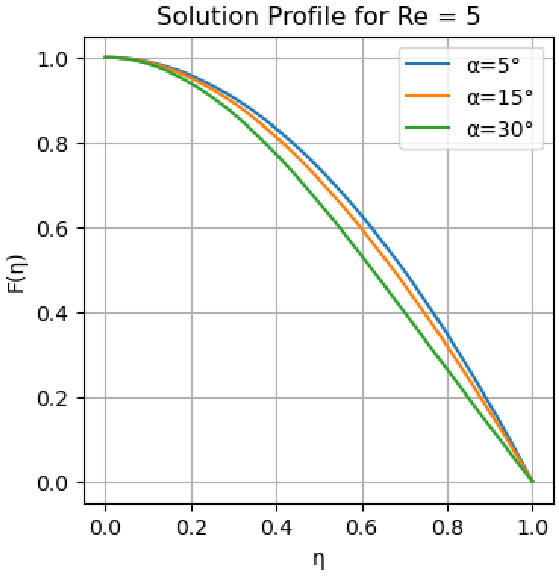

Fig. 17 Plot comparison of $F(\eta)$ for different positive angles when $Re = 5$.

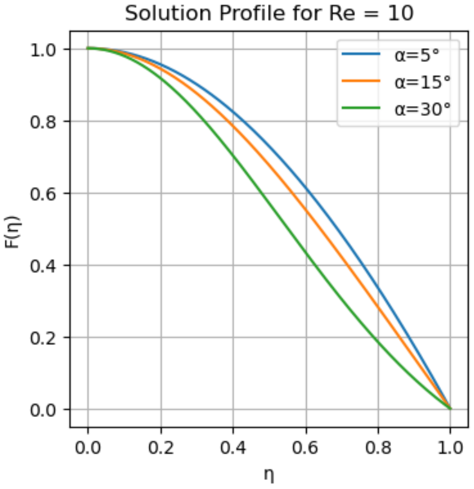

Fig. 18 Plot comparison of $F(\eta)$ for different positive angles when $Re = 10$.

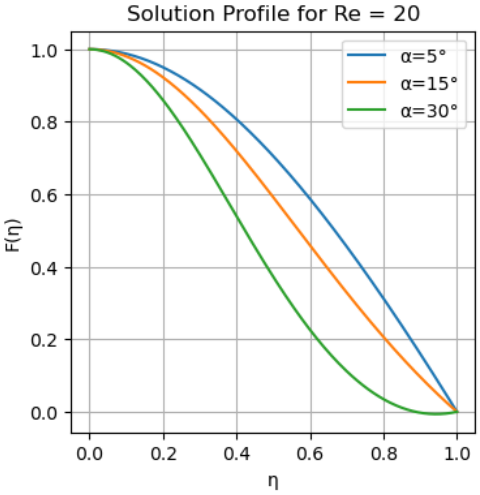

Fig. 19 Plot comparison of $F(\eta)$ for different positive angles when $Re = 20$.

4.2.2 Plot comparison of $\boldsymbol{F(\eta)}$ for different $\boldsymbol{Re}$ at fixed angles

This subsection examines the effect of increasing the Reynolds number on the average fluid velocity at a fixed angle. Contrary to initial expectations, in a divergent channel with fixed wall angles, a higher Reynolds number results in a decrease in the average fluid velocity. Furthermore, Figures 20–22 indicate that an increase in the channel's wall angle leads to a more pronounced reduction in velocity. In summary, at a specific wall angle, a higher Reynolds number corresponds to a lower average velocity, while within a fixed Reynolds number range, a larger wall angle further reduces the average velocity. These trends are quantitatively presented in Tables 5–7.

Table 5 The quantitative results for different Reynolds numbers when $\alpha = 5°$.

Re	F_{avg} (Average $F(\eta)$)	% Change (vs $Re = 5$)
5	0.659	0.0%
1·	0.652	-1.1%
20	0.637	-3.4%

Table 6 The quantitative results for different Reynolds numbers when $\alpha = 15°$.

Re	F_{avg} (Average $F(\eta)$)	% Change (vs $Re = 5$)
5	0.641	0.0%
1·	0.617	-3.7%
20	0.564	-12.0%

Table 7 The quantitative results for different Reynolds numbers when $\alpha = 30°$.

Re	F_{avg} (Average $F(\eta)$)	% Change (vs $Re = 5$)
5	0.606	0.0%
1·	0.550	-9.1%
20	0.431	-28.8%

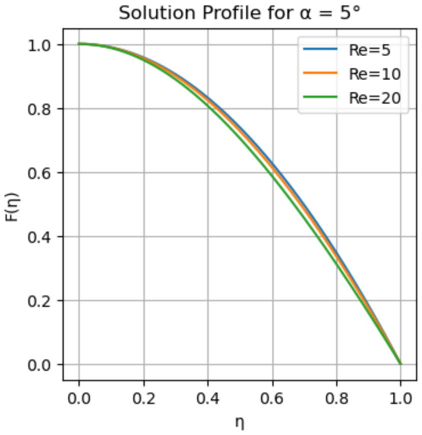

Fig. 20 Plot comparison of $F(\eta)$ for different Reynolds numbers when $\alpha = 5°$.

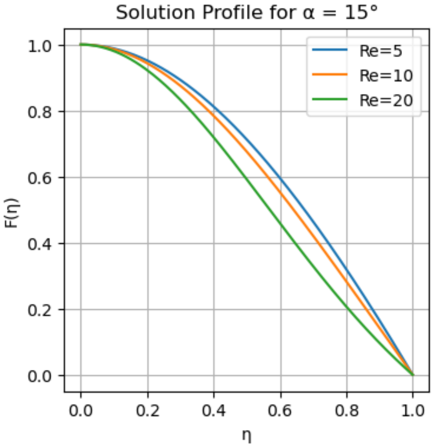

Fig. 22 Plot comparison of $F(\eta)$ for different Reynolds numbers when $\alpha = 15°$.

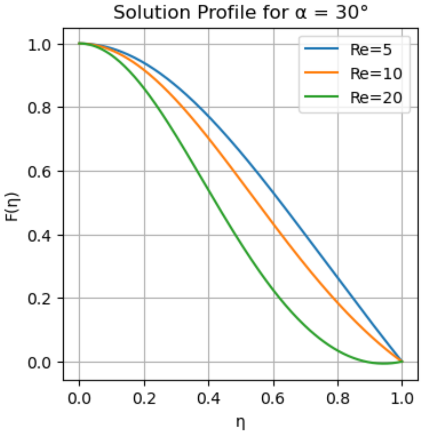

Fig. 22 Plot comparison of $F(\eta)$ for different Reynolds numbers when $\alpha = 30°$.

4.3 Impact of Reynolds number and angle of wall in a convergent channel

4.3.1 Plot comparison of $\boldsymbol{F(\eta)}$ for different negative angles at fixed $\boldsymbol{Re}$

In this subsection, a convergent channel configuration is examined. For a given Reynolds number, increasing the wall angle (i.e., increasing the magnitude of the negative angle) results in an increase in the average fluid velocity. Conversely, at a fixed Reynolds number, decreasing the wall angle leads to a reduction in the average velocity. This behavior is clearly illustrated in Figures 23–25, with corresponding quantitative results presented in Tables 8–10. Furthermore, the data indicate that the sensitivity of the average velocity to changes in the wall angle is more pronounced at higher Reynolds numbers. In other words, for a fixed channel angle, higher Reynolds numbers yield higher average fluid velocities, and the enhancement of velocity with increasing convergence becomes even more significant as the Reynolds number increases.

Table 8 The quantitative results for for different negative angles when $Re = 5$.

α (deg)	F_{avg} (Average $F(\eta)$)	% Change (vs $\alpha = -5°$)
-5	0.673	0.0%
-15	0.684	1.6%
-30	0.694	3.2%

Table 9 The quantitative results for for different negative angles when $Re = 10$.

α (deg)	F_{avg} (Average $F(\eta)$)	% Change (vs $\alpha = -5°$)
-5	0.680	0.0%
-15	0.702	3.3%
-30	0.727	7.0%

Table 10 The quantitative results for for different negative angles when $Re = 20$.

α (deg)	F_{avg} (Average $F(\eta)$)	% Change (vs $\alpha = -5°$)
-5	0.692	0.0%
-15	0.733	5.9%
-30	0.776	12.0%

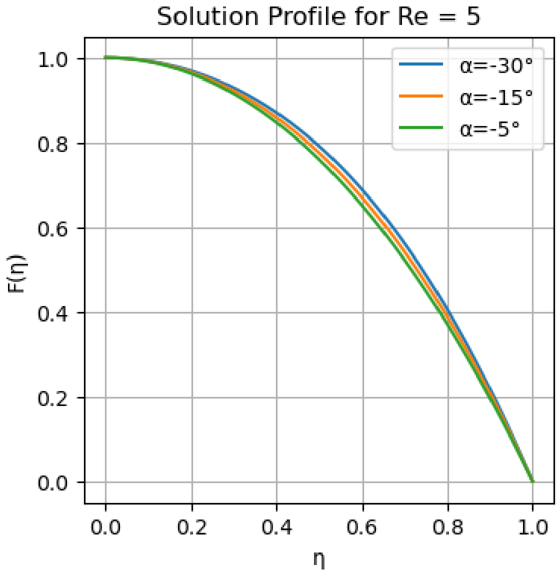

Fig. 23 Plot comparison of $F(\eta)$ for different negative angles when $Re = 5$.

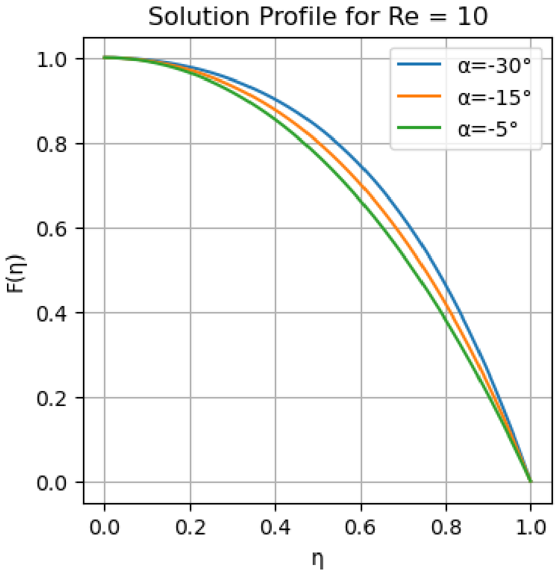

Fig. 24 Plot comparison of $F(\eta)$ for different negative angles when $Re = 10$.

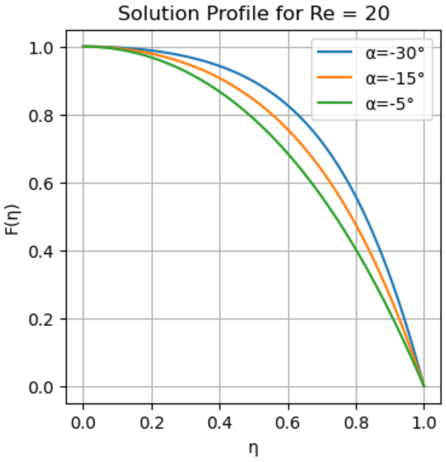

Fig. 25 Plot comparison of $F(\eta)$ for different negative angles when $Re = 20$.

4.3.2 Plot comparison of $\boldsymbol{F(\eta)}$ for different $\boldsymbol{Re}$ at fixed angles

Figures 26–28 and Tables 11–13 indicate that, in a convergent channel at a given angle, an increase in Reynolds number results in a higher velocity, in contrast to a divergent channel. Moreover, as the convergence angle (or the wall angle) increases, the average fluid velocity also increases. In summary, for a converging channel, both a larger convergence angle and a higher Reynolds number lead to an increase in the average velocity. Quantitative details of these results are provided in Tables 11–13.

Table 11 The quantitative results for different Reynolds numbers when $\alpha = -5°$.

Re	F_{avg} (Average $F(\eta)$)	% Change (vs $Re = 5$)
5	0.673	0.0%
1٠	0.680	1.0%
20	0.692	2.9%

Table 12 The quantitative results for different Reynolds numbers when $\alpha = -15°$.

Re	F_{avg} (Average $F(\eta)$)	% Change (vs $Re = 5$)
5	0.684	0.0%
1٠	0.702	2.7%
20	0.733	7.3%

Table 13 The quantitative results for different Reynolds numbers when $\alpha = -30°$.

Re	F_{avg} (Average $F(\eta)$)	% Change (vs $Re = 5$)
5	0.694	0.0%
1٠	0.727	4.7%
20	0.776	11.7%

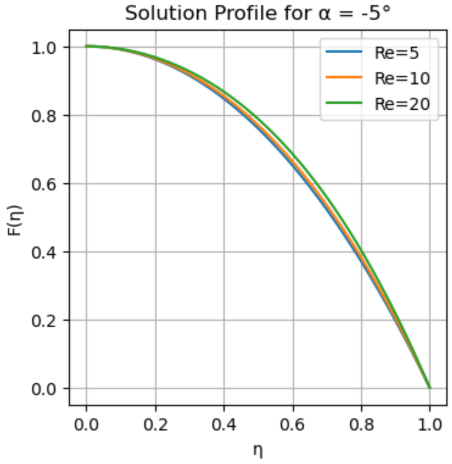

Fig. ٢26 Plot comparison of $F(\eta)$ for different Reynolds numbers when $\alpha = -5°$.

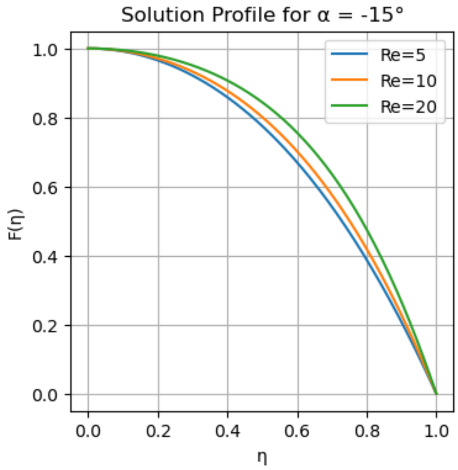

Fig. 27 Plot comparison of $F(\eta)$ for different Reynolds numbers when $\alpha = -15°$.

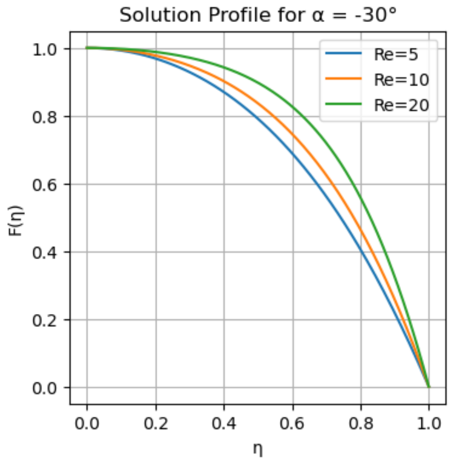

Fig. 28 Plot comparison of $F(\eta)$ for different Reynolds numbers when $\alpha = -30°$.

5 Conclusion

This study demonstrates how numerical solutions to differential equations can be refined and systematically transformed into analytical expressions through a five-step methodology of HAN method. The nonlinear ordinary differential equation (ODE) employed in this study is the Jeffery-Hamel equation, which serves as a mathematical model for fluid flow within divergent and convergent channels. The derivation of this ODE is presented in Section 2.2. To summarize the key findings of this research, the following bullet points outline the mathematical and physical conclusions derived from this study.

- Innovative Hybrid Approach: The HAN method uniquely transforms numerical solutions into analytical forms, addressing convergence issues and avoiding excessive terms in existing semi-analytical solutions.
- Flexibility in Numerical Integration: It adapts to different numerical methods when standard approaches fail, ensuring robust solutions for nonlinear differential equations.
- Systematic Five-Step Process:
    - Step 1: Propose an analytical solution (e.g., polynomial) with undetermined coefficients.
    - Step 2: Derive algebraic equations from boundary conditions (BCs).
    - Step 3: Supplement BCs with approximated conditions from numerical solutions.
    - Step 4: Derive the remaining algebraic equations from approximated BCs.
    - Step 5: Solve the system of linear algebraic equations and obtain a semi-analytical solution.
- Adaptive Boundary Conditions: Uses numerical solutions to generate additional constraints when BCs are insufficient, ensuring solvability.
- Implicit Validation: Assumes solution validity during steps 3–5 but supports accuracy via:
    - Numerical convergence checks.
    - Residual error analysis by substituting the HAN solution back into the original equation.
- Implementation & Verification:
    - Employed Runge-Kutta in Python for numerical solutions.
    - Confirmed convergence and negligible residuals to validate results.
- Reliability and Precision: Combines numerical and analytical strengths, offering concise, accurate solutions for complex problems.
- Increasing wall angles in a divergent channel leads to a decrease in average fluid velocity.
- In a divergent channel, the reduction in velocity is more pronounced at higher Reynolds numbers.
- Conversely, in a divergent channel, decreasing wall angles or approaching a configuration with approximately flat walls, increases the average fluid velocity.
- Jeffery–Hamel's equation (Eq. 20) is applicable only for convergent ($\alpha < 0$) or divergent ($\alpha > 0$) channels—not at angles of 0°, 90°, 180°, or 360°.
- At a fixed wall angle in a divergent channel, increasing the Reynolds number results in a lower average fluid velocity.
- In a divergent channel, a larger wall angle further intensifies the reduction in velocity within a given Reynolds number range.
- For a given Reynolds number, in the convergent channels, increasing the wall angle (i.e., increasing the magnitude of the negative angle) results in a higher average fluid velocity.
- Conversely, decreasing the wall angle in the convergent channels leads to a reduction in average velocity.
- In the convergent channels, the sensitivity of average velocity to wall angle variations is more pronounced at higher Reynolds numbers.
- Both a larger convergence angle and an increased Reynolds number in a convergent channel, lead to a higher average fluid velocity.

Nomenclature

Non-Greek letters

$\hat{\mathbf{r}}$	Unit vector along r-axis, (-)
r	Radial coordinate, (m)
z	Axial coordinate, (m)
$\mathbf{u}$	Velocity vector of the fluid, (m/s)
$\mathbf{F}$	Body force per unit volume, $(\mathrm{N/m^3})$
$u_r, u_r(r,\theta)$	Radial velocity component, (m/s)
$u_\theta, u_\theta(r,\theta)$	Angular velocity component, (m/s)
$p, p(r,\theta)$	Pressure distribution, (Pa)
$f(\theta)$	Dimensional function in terms of θ, $(\mathrm{m^2/s})$
$F(\eta)$	Dimensionless form of $f(\theta)$, (-)
Re	Reynolds number, (-)
U_{char}	Characteristic velocity, (m/s)
$U_{\max}$	Maximum velocity of the fluid, (m/s)
L_{char}	Characteristic length, (m)

Greek letters

$\hat{\boldsymbol{\theta}}$	Unit vector along θ-axis, (-)
θ	Angular coordinate, (m)
ρ	Fluid density, $(\mathrm{kg/m^3})$
μ	Dynamic viscosity, $(\mathrm{kg/m\cdot s})$
ν	Kinematic viscosity, $(\mathrm{m^2/s})$
α	Half-angle or angle of each wall with r-axis, (Degree or Radian)
η	Independent dimensionless similarity variable, (-)

Mathematics

∇	Gradient operator, (unit per meter)
$\nabla\cdot$	Divergence operator, (unit per square meter)
∇^2	Laplace operator, (unit per square meter)
$\mathrm{D}/\mathrm{D}t$	Total derivative with respect to time, (unit per second)

References

1. P. Jalili, A. Ahmadi Azar, B. Jalili, Z. Asadi, D. D. Ganji, *Case Studies in Thermal Engineering* **40** (2022)
2. P. Jalili, A. Ahmadi Azar, B. Jalili, D. Domiri Ganji, *Results Phys.* **48**, 106371 (2023)
3. P. Jalili, A. Ahmadi Azar, B. Jalili, D. Domiri Ganji, *Heliyon* **9**, e17535 (2023)
4. P. Jalili, A. Ahmadi Azar, B. Jalili, D. Domiri Ganji, *Scientific Reports* **13**, 13241 (2023)
5. B. Jalili, A. Ahmadi Azar, P. Jalili, D. Domiri Ganji, *Alex. Eng. J.* **79**, 196-226 (2023)
6. E. Ahmadi Azar, B. Jalili, A. Ahmadi Azar, M. Atazadeh, D. Domiri Ganji, *Phys. Dark Universe* **42,** 101309 (2023)
7. B. Jalili A. Ahmadi Azar, P. Jalili, D. Domiri Ganji, *Case Studies in Thermal Engineering* **52**, 103672 (2023)
8. A. Ahmadi Azar, B. Jalili, P. Jalili, D. Domiri Ganji, *Scientific Reports* **13**, 21833 (2023)
9. B. Jalili, A. Ahmadi Azar, K. Esmaeili, D. Liu, P. Jalili, D. Domiri Ganji, *Chinese Journal of Physics* **87**, 118-137 (2024)
10. P. Jalili, A. Ahmadi Azar, B. Jalili, D. Domiri Ganji, *Arab. J. Sci. Eng.* **49**, 10453-10469 (2024)
11. A. Ahmadi Azar P. Jalili, Z. P. Moziraji, B. Jalili, D. Domiri Ganji, *Heliyon* **10**, e34888 (2024)
12. B. Jalili A. Ahmadi Azar, P. Jalili, D. Liu, M. A. H.- Abdelmohimen, D. Domiri Ganji, *Case Studies in Thermal Engineering* **61**, 104859 (2024)
13. B. Jalili, A. Ahmadi Azar, D. Liu, P. Jalili, C. Kang, D. Domiri Ganji, *Phys. Fluids* **36**, 113129 (2024)
14. N. Heidari, M. de Montigny, A. Ahmadi Azar, T. Sathiyaraj, H. Hassanabadi, *Nucl. Phys. B* **1009**, 116750 (2024)
15. A. Ahmadi Azar, P. Jalili, B. Jalili, D. Domiri Ganji, *Multidiscipline Modeling in Materials and Structures* **21**, 68-97 (2025)
16. A. Ahmadi Azar, *Mechanical Engineering Advances* **3**, 2878-2878 (2025)
17. A. Ahmadi Azar, *Int. Commun. Heat Mass Transf.* **165**, Part A, 109040 (2025)
18. A. Bejan, Convection heat transfer, John wiley & sons, (2013)
19. H. Schlichting, K. Gersten, Boundary-layer theory, New York: McGraw-Hill, (2000)
20. A. A. Joneidi, G. Domairry, M. Babaelahi. *Commun. Nonlinear Sci. Numer. Simul.* **15**, 3423-3434 (2010)
21. H. S. Patel, R. Meher. *Ain Shams Eng. J.* **9**, 599-606 (2018)
22. A. Dib, A. Haiahem, B. Bou-Said, *Comput. Fluids* **102**, 111-115 (2014)
23. D. Domiri Ganji, M. Sheikholeslami, H. R. ejad., *International Scholarly Research Notices* **1**, 937830 (2011)
24. J. Singh, Y. S. Shishodia. *J. Assoc. Arab Univ.* **16**, 11-15 (2014)
25. Z. Asghar, R. S. Saif, N. Ali, *Alex. Eng. J.* **61,** 4479-4490 (2022)
26. L. Lu, J. Duan, L Fan, *Adv. Appl. Math. Mech.* **7**, 675-686 (2015)
27. L. Bougoffa., S. Mziou, R. C. Rach, *Mathematical Modelling and Analysis*, **21,** 174-187 (2016)
28. Q. Esmaili, A. Ramiar, E. Alizadeh, D. Domiri Ganji, *Phys. Lett. A* **372**, 3434-3439 (2008)
29. A. Mahmood, M. F. Md Basir, U. Ali, M. S. Mohd Kasihmuddin, M. A. Mansor, *Processes* **7**, 626 (2019)
30. U. Khan, W. Sikandar, N. Ahmed, S. T. Mohyud-Din., *Int. J. Comput. Math.* **2**, 469-483 (2016)
31. R. Meher, N. D. Patel. *SN Appl. Sci.* **1**, 656 (2019)